

DUST ECHOES FROM THE AMBIENT MEDIUM OF GAMMA-RAY BURSTS

Kevin Heng¹, Davide Lazzati¹ & Rosalba Perna¹

ABSTRACT

Long gamma-ray bursts (GRBs) are likely associated with the collapse of massive stars, which produce dust and are born in dusty environments. Absorption and scattering of ultraviolet/X-ray photons from the prompt, optical flash and afterglow emission of the GRB produce dust echoes. We perform time-dependent calculations of these echoes, accounting for the evolution of the dust grain distribution due to selective grain destruction by the GRB radiation, and for off-axis beaming. We explore cloud configurations of differing density and size — the echo light curve and spectrum depend on the cloud radius, with larger clouds peaking at longer wavelengths. For a region ~ 3 pc in size with density $n_{\text{H}} \sim 10^3$ cm^{-3} , the echo spectrum peaks at ~ 3.6 μm and ~ 8.8 eV for thermal and scattered components, respectively. Dust echoes should be detectable with the *Very Large Telescope* up to $z \sim 0.1$, IRAC onboard the *Spitzer Space Telescope* up to $z \sim 0.2$, and NICMOS onboard the *Hubble Space Telescope* up to $z \sim 0.3$. Furthermore, the shape of the echo light curve allows one to infer: the jet opening angle; the inclination of the jet axis with respect to the line of sight; the size of the dust-emitting region. For sources with symmetric, bipolar jets, dust echoes exhibit two bumps in the light curve, making them easily distinguishable from the rebrightening due to an underlying supernova.

Subject headings: gamma-rays: bursts — radiative transfer — ISM: dust

1. INTRODUCTION

Dust echoes are produced when photons emitted from a source (nova, supernova, quasar, gamma-ray burst, etc) interact with the ambient dust grains, which either scatter or thermally re-emit the photons and divert some of them towards the observer. These photons may be observed long after the source has faded, thus providing a way of studying both the

¹JILA, University of Colorado, 440 UCB, Boulder, CO 80309-0440; hengk@colorado.edu

nature of the source and its surroundings. A number of papers have been written on dust echoes, including those by Dwek (1983), Chevalier (1986), Milgrom (1987), Schaefer (1987a, b), Emmering & Chevalier (1989), Sparks (1994), Xu, Crotts & Kunkel (1994, 1995), Sugerman (2003) and Patat (2005, hereafter P05), following pioneering work by Couderc (1939). All of these papers deal with the dust echoes — also called “light echoes” — produced by static dust distributions illuminated by a relatively weak flux of radiation. In gamma-ray bursts (GRBs), the radiation flux is so large that dust can be destroyed out to ~ 10 pc by ultraviolet (UV) and X-ray heating, ion field emission (IFE; Waxman & Draine 2000, hereafter WD00) or Coulomb explosions (Fruchter, Krolik & Rhoads 2001).

The modeling of dust echoes in GRBs is therefore complicated by the need to perform a time-dependent treatment of the dust, where temperatures and size distributions evolve as a function of time and distance from the source. Dust grains are selectively destroyed according to their size and chemical composition, making it impossible to define a destruction radius uniquely. Previous work either relied on neglecting the dust evolution or assumed a destruction radius within which all of the dust is destroyed and beyond which it is unaffected. These include the work of WD00, Esin & Blandford (2000, hereafter EB00), Reichart (2001, hereafter R01), Venemans & Blain (2001) and Moran & Reichart (2005, hereafter MR05).

The motivation for considering GRB dust echoes originates from researchers wanting to provide an alternative interpretation of the evidence for a GRB/supernova connection (e.g., WD00; EB00; R01) and to explain color fluctuations in afterglow light curves (MR05). With the discovery of the association between long GRBs and the collapse of massive stars (Hjorth et al. 2003; Stanek et al. 2003), the alternative explanation for supernova (SN) bumps is no longer necessary. However, since massive stars have relatively short lifetimes, the majority of them are expected to die within the dense and dusty molecular clouds in which they were created. Dense environments, with conditions comparable to those in molecular cloud cores, have indeed been inferred in a few cases (Lazzati & Perna 2002; Frontera et al. 2004; Frail et al. 2006). The study of dust echoes from GRBs then becomes motivated by the fact that they provide a three-dimensional map of the geometry of the emitting region. For an isotropic dust distribution, this in turn translates into a geometric mapping of the source of radiation, constituting an independent way of constraining the degree of beaming of GRB jets.

In this paper, we present significant improvements to existing models of dust echoes by combining time-dependent echo calculations, which are able to account for off-axis, bipolar GRB beaming, with a code that follows the evolution of the dust grain population. The photoionization and dust destruction code, written by Perna & Lazzati (2002, hereafter PL02; see also Perna, Lazzati & Fiore 2003 and Lazzati & Perna 2003), models the destruction of

dust grains due to UV and X-ray sublimation, as well as IFE. Evolution of the (graphite and silicate) grains, hydrogen and the 12 most abundant metals are self-consistently combined. The mono-dimensional output of the dust code is subsequently fed to a three-dimensional echo code that computes the contribution of the dust populations to the thermal and scattered echoes. In §2, we discuss the dust echo geometry and GRB parameters adopted, and describe our use of the PL02 code. We present our results in §3 and discuss their implications in §4.

2. METHODS

2.1. ECHO GEOMETRY

We adopt the dust echo geometry of Sugerman (2003) and consider a coordinate system in which a thin, planar sheet of dust, of thickness dz , is located a distance z away from the source (Fig. 1). From the point of view of the observer, an echo of projected radius ρ and width $d\rho$ is seen. Dust grains, each located a distance r from the source, scatter the light onto parabolic surfaces (Couderc 1939):

$$z = \frac{\rho^2}{2ct} - \frac{ct}{2}. \quad (1)$$

Suppose an isotropic burst of energy (per unit frequency), $E_{\nu,\text{input}} = E_{\nu,\text{input}}(\nu, t)$, is released by the source at a time t_0 , over some (global) time interval $\delta t = t - t_0$ and at a frequency ν , such that $L_{\nu,\text{input}} = E_{\nu,\text{input}}/\delta t$. We first calculate the integrated, monochromatic luminosity, $L_{\nu,\text{sc}} = L_{\nu,\text{sc}}(\nu, t)$, due to scattering, at some time t after the burst. If a denotes the grain size and $n = n(a, r, t)$ is the dust density,

$$L_{\nu,\text{sc}} = \int \int_V \frac{L_{\nu,\text{input}} a^2 Q_{\text{sc}} \Phi}{4 r^2} \frac{dn}{da} \frac{\delta t}{\Delta t} dV da, \quad (2)$$

where $Q_{\text{sc}} = Q_{\text{sc}}(a, \nu)$ is the scattering efficiency and $dV = 2\pi\rho d\rho dz$ is the echo volume element in the absence of beaming. The *local* time interval, Δt , is the time lag between successive echo parabolic surfaces. In practice, we follow the evolution of the dust grains in discrete bins of Δa (see §2.4). The Henyey & Greenstein (1941, hereafter HG41) phase function takes the form

$$\Phi = \frac{1 - g^2}{(1 + g^2 - 2g\mu)^{3/2}}, \quad (3)$$

with $g = g(a, \nu)$ characterizing the degree of forward scattering for a given grain. The quantity $\mu = z/r$ is the cosine of the scattering angle, θ . In almost all of the work cited, the

HG41 phase function is adopted. P05 notes that more sophisticated calculations, such as a full Mie treatment, show that the HG41 formulation tends to underestimate the forward scattering, but the approximation is reasonably good.

For thermal re-emission, the integrated, monochromatic luminosity is

$$L_{\nu,\text{th}} = \int \int_V 4\pi^2 a^2 B_\nu Q_{\text{abs}} \frac{dn}{da} \frac{\delta t}{\Delta t} dV da, \quad (4)$$

where $Q_{\text{abs}} = Q_{\text{abs}}(a, \nu)$ is the absorption efficiency and $B_\nu = B_\nu(T(a, r, t), \nu)$ is the Planck or blackbody intensity. Collectively, the monochromatic light curve observed is given by

$$L_\nu = L_{\nu,\text{sc}} + L_{\nu,\text{th}}. \quad (5)$$

Though we use a planar slab for the purpose of illustration, our formalism can be applied to any geometry. Analytical formulae for the simple cases of a slab and a spherical shell are given in, for example, P05. Tabulated values for g , Q_{sc} and Q_{abs} are provided by Draine & Lee (1984) and Laor & Draine (1993).

In our case, we consider a bipolar jet of opening half-angle θ_{jet} , positioned at a viewing angle ψ between the jet axis and the line of sight (Fig. 2). The cosine of the occurrence angle, θ' , is given by

$$\cos \theta' = \cos \theta \cos \psi + \sin \theta \sin \psi \cos \phi. \quad (6)$$

The luminosity contribution from a given dust grain is only included when either the condition $\theta' < \theta_{\text{jet}}$ or $\theta' > \pi - \theta_{\text{jet}}$ is satisfied. The echo volume element is then generalized to $dV = \rho d\phi d\rho dz$ and there is an additional integration over the azimuthal angle, ϕ . Again, in practice, one sums over discrete intervals or bins of $\Delta\rho$, $\Delta\phi$, Δz and Δa .

2.2. GRB LIGHT CURVE MODELING

The GRB light curve has three components: the prompt emission, an optical flash and the afterglow (Fig. 3). We model the prompt emission as

$$L_{\nu,\text{pm}}(\nu, t) = \frac{L_0}{1 + (\nu/6 \times 10^{19} \text{ Hz})^{2.5}} \begin{cases} \exp(-3 + t/1 \text{ s}) & , t \leq 3 \text{ s} \\ \exp(0.3 - t/10 \text{ s}) & , t \geq 3 \text{ s}. \end{cases} \quad (7)$$

The quantity $L_0 = 1.16 \times 10^{32} \text{ erg s}^{-1} \text{ Hz}^{-1}$ is chosen such that $\int \int L_{\nu,\text{pm}} d\nu dt \approx 10^{53} \text{ erg}$.

We allow for the presence of an optical flash, as observed in GRB 990123 (Akerlof et al. 1999), modeled through the function (e.g., Draine & Hao 2002)

$$L_{\nu,\text{of}} = 3 \times 10^{33} \text{ erg s}^{-1} \text{ Hz}^{-1} \frac{(t/30 \text{ s})^{3/2}}{1 + (t/30 \text{ s})^{7/2}} \begin{cases} (\nu/4 \times 10^{14} \text{ Hz})^{-0.65} & , \nu < \nu_B \\ 100^{-0.65} \exp(\nu/\nu_B - 1) & , \nu \geq \nu_B \end{cases} \quad (8)$$

where $\nu_B = 8 \times 10^{17} \text{ Hz}$.

For the afterglow, we use (Panaitescu & Kumar 2000)

$$L_{\nu,\text{ag}} = 3 \times 10^{33} \text{ erg s}^{-1} \text{ Hz}^{-1} \left[(t/30 \text{ s})^{-0.5} + (t/30 \text{ s})^{1.125/6} \right]^{-6} \left(\frac{\nu}{4 \times 10^{14} \text{ Hz}} \right)^{-1.15}. \quad (9)$$

It follows that the input luminosity (per unit frequency) from the GRB is

$$L_{\nu,\text{input}} = L_{\nu,\text{pm}} + L_{\nu,\text{of}} + L_{\nu,\text{ag}}. \quad (10)$$

Figure 3 shows the R band light curve according to our model for a GRB at $z = 1$. If the GRB ejecta are beamed, then the afterglow eventually evolves to $L_{\nu,\text{ag}} \propto t^{-p}$, where $p = 2.5$ is the index of the electron energy distribution, $F(\epsilon) \propto \epsilon^{-p}$, at a time

$$t_{\text{break}}(\theta_{\text{jet}}) = \left(\frac{3E}{4\pi c^5 m_H n} \right)^{1/3} \theta_{\text{jet}}^{8/3}, \quad (11)$$

where $E = 10^{53} \text{ erg}$ and n is the number density of the ambient gas. In the case of an off-axis jet, we adopt the following approximation: at $t_{\text{break}} = t_{\text{break}}(\psi)$ (Rossi, Lazzati & Rees 2002; Zhang & Mészáros 2002), $L_{\nu,\text{ag}}$ transitions from $\propto t^2$ to $\propto t^{-p}$; we ignore the $\propto t^3$ and plateau behaviors just before t_{break} .

2.3. DUST MODELING

As discussed in §1, the massive-star progenitors of GRBs — probably of the Wolf-Rayet type — are likely to die close to the locations where they were born, in dense, molecular cloud cores. While we compute the peaks of the dust echo emission for different cloud configurations, we focus most of the calculations on a typical example of such a cloud; specifically, one with radius $R = 3 \text{ pc}$ and hydrogen column density $N_{\text{H}} = 10^{22} \text{ cm}^{-2}$, corresponding to $n_{\text{H}} \sim 10^3 \text{ cm}^{-3}$ or, equivalently, a gas mass of $\sim 1000 M_{\odot}$. The GRB is assumed to be located at the center of the cloud. Since late-type WC stars are themselves known to be dust-making machines (e.g., Williams, van der Hucht & The 1987), a further concentration of dust is expected in the vicinity of the star. Observations by Williams, van

der Hucht & The (1987) indicate these distances to be $\sim 10^{14}$ to 10^{15} cm. MR05 considered specifically the emission from this proximate dust layer, showing that it yields a peak emission within a few minutes after the burst. We consider a uniform distribution of dust within the molecular cloud, with a solar dust-to-gas mass ratio, $f_{\odot} = 0.01$.

A variety of grain models exist and the interested reader is referred to, for example, the review by Draine (2004). In general, they incorporate a combination of silicates, graphite and polycyclic aromatic hydrocarbons (PAHs). Broadly speaking, the presence of graphite grains may account for the 2175 Å bump in the extinction curve. Steep UV extinction may be due to the presence of silicate grains. PAHs account for several unique emission features, as well as for far ultraviolet extinction. Various types of composite grains may also provide the bulk of the infrared and optical extinction. We specialize to Galactic-type dust, which is believed to be a mixture of graphite and silicate grains — with the latter having an average composition of MgFeSiO_4 , also known as “olivine”; see Draine & Lee (1984) — following Mathis, Rumpl & Nordsieck (1977). We assume an initial, power-law distribution

$$\frac{dn}{da} \propto a^{-\beta}, \quad (12)$$

where $\beta = 3.5$. While this value of β is typical of the dust found in our Galaxy, it might not accurately represent the grain distributions in denser environments. Nevertheless, it is a good first approximation. As the burst radiation propagates through the medium, the grain population evolves and β either changes or ceases to be meaningful as portions of the distribution may be completely destroyed. Dust echoes probe the distribution of dust while it is being modified by the burst radiation. We properly compute the temporal evolution of the dust distribution, as described in the succeeding sub-section.

2.4. DUST EVOLUTION

As mentioned in §1, we follow the evolution of dust as a function of position within the cloud by using the dust code of PL02, which treats metals (He, C, N, O, Ne, Mg, Si, S, Ar, Ca, Fe, Ni), hydrogen (in all of its atomic and molecular forms) and dust evolution in a self-consistent manner. For dust destruction, UV and X-ray sublimation and IFE are considered. Sublimation occurs when grains absorb energy faster than they manage to radiate away and the excess energy goes into breaking the bonds that hold the atoms to the surface of the grain. Small and large grains are heated predominantly by UV radiation and X-rays, respectively.

IFE occurs when a grain is charged up to a potential of $V_{\max} = 3a_{-5}(S/10^{11} \text{ dyn cm}^{-2})^{1/2}$ kV, where $a = a_{-5}10^{-5}$ cm and S is the tensile strength of the grain material, and any further ionization leads to the emission of ions in order to avoid an increase in the surface electric

field. The process of Coulomb explosion, which is the fragmentation of the grain into smaller components, competes with that of IFE. The relative importance of the two processes is a subject of controversy. PL02 adopt the approach of Draine & Hao (2002) and assume that Coulomb explosion does not play a major role, due to the possibility of chemical bonds being promptly re-established in the warm grain — annealing. Grains close to the source are sublimated, while those far away from it are eroded by IFE.

As dust destruction fronts propagate, dust-depleted metals are recycled into gas. As such, their abundances in the gaseous and the dust-depleted phases are book-kept separately. Computationally, at each time step t , the code calculates dn/da and T as a function of both r and a [Fig. 4; see also Perna, Lazzati & Fiore (2003) for further examples of dust evolution for various initial values of β]. In this way, the dust populations are evolved both spatially and temporally. We see from Fig. 4 that graphite grains are more resistant to the impinging radiation; larger grains tend to survive better as well.

2.5. CLOUD OPACITY

Neither the dust code of PL02 nor our echo code deals with the multiple-scattering effects of radiative transfer in an optically-thick cloud. There are three regimes of opacities, namely clouds that are: optically thin at the beginning of the burst; optically thick at the end of the burst and afterglow; initially optically thick but become optically thin after part of the dust is destroyed by the burst and afterglow radiation. Certainly, this definition is dependent on wavelength.

Clouds that are initially optically thin to radiation are not a concern, since multiple scattering and absorption/re-emission are negligible. However, a cloud can be optically thin in the infrared but thick in the UV; in principle, UV radiation can be “downgraded” to the infrared by multiple scattering and absorption/re-emission events, thus contributing to the infrared lightcurve. However, this effect is small for two reasons. Firstly, the dust temperatures at long time scales are low, due to the rapid cooling of the grains. UV radiation will be reprocessed in the far infrared, at wavelengths $\sim 10 \mu\text{m}$, much longer than those considered below. Secondly, although multiple scattering will introduce a time dilution effect to the light curve (by delaying the photons and causing them to be detected at later times), we expect it to be small. The ratio of the contributions from the multiply-scattered component to the singly-scattered one is $\sim \tau \exp(-\tau)$; for large optical depths ($\tau \gg 1$), extinction dominates over time dilution, making the multiply-scattered component negligible.

To understand how to deal with initially opaque clouds, we must examine in detail the

process of dust sublimation and the relative time scales. The former (due to heating) is driven by the burst flux. Therefore it takes place during the GRB prompt phase, which lasts ~ 10 s. The slower IFE process, which is driven by the burst fluence, lasts for several hours up to a maximum of a few days. The dust destruction process takes place within a thin shell of thickness $\delta R \lesssim 10^{15}$ cm, a tiny fraction of the cloud radius. Therefore, to a very good approximation, the dust destruction front propagates at the speed of light. Consider now a photon that is re-directed towards some line of sight. Due to the time delay in its propagation, it will be lagging behind the front. As a consequence, it will propagate only through the post-burst dust population. To compute the number of photons, a time-dependent dust treatment is required, but only the final configuration of the cloud is necessary to evaluate the extinction of the thermally re-emitted and scattered light.

This allows us to develop a very simple recipe to deal with isotropic bursts. Regardless of the initial opacity in the band considered, we can compute the echo light curve ignoring the opacity and eventually correct *a posteriori* with the residual extinction (if any). A more complex treatment is necessary for beamed GRBs. As shown in Fig. 5, a beamed GRB cleans out only a biconical region of the cloud and, for any initially-opaque cloud, a proper treatment of the opacity has to be included. A simple one is not possible in this case since, as shown in the figure, different amounts of dust lie along different lines of sight. The treatment becomes even more complicated for off-axis observers, due to the loss of the cylindrical symmetry. For this reason we restrict our treatment of beamed GRB echoes to initially optically-thin clouds.

3. RESULTS

3.1. LIGHT CURVES & SPECTRA

Dust echoes have a duration $t_{\text{echo}} \sim 2R/c$ and the energy involved is $E_{\text{echo}} \sim \zeta E$. The “echo efficiency factor”, ζ , depends on the total amount of dust present in the scattering and thermally re-emitting region, the distance of the dust from the burst, the dust composition and the GRB spectrum. The dependence of ζ on the GRB and cloud parameters is complex. A large value of ζ can be achieved if the dust grains are sufficiently far away to survive fast sublimation by the burst photons, yet close enough to be heated to high temperatures and provide a sizable optical depth. Dust grains in the path of the optical-UV flash are expected to be sublimated out to a distance ~ 1 pc (WD00). Using the PL02 dust code described in §2.4, we follow the evolution of dust grains, with sizes $0.3 \text{ nm} \lesssim a \lesssim 0.3 \text{ }\mu\text{m}$, for various values of the density and radius of the absorbing cloud.

Figure 6 shows how the wavelength of the peak emission, for the thermal and scattered components, varies as a function of the cloud parameters. The general trend is for it to increase with cloud size (Fig. 6); since the temperature of the dust declines with distance from the radiation source, larger clouds have higher fractions of cooler dust. On the other hand, for a fixed radius, the peak of the emission is density-independent as long as the cloud is optically thin (for $N_{\text{H}} = 10^{21}$ and 10^{22} cm^{-3}), but it shifts to longer wavelengths when the cloud becomes optically thick ($N_{\text{H}} = 10^{23}$ cm^{-3}). This is due to the fact that if the cloud is optically thick, less radiation propagates to the outer layers of dust, and therefore the grains attain a lower temperature.

For the remainder of the paper, unless otherwise noted, we will concentrate on the (optically thin) case of a cloud with radius $R = 3$ pc and $N_{\text{H}} = 10^{22}$ cm^{-3} . Figure 7 shows echo light curves for the source/rest wavelength $\lambda_0 = 3.55$ μm — we will justify our choice shortly — for various values of the jet opening half-angle; the line of sight is coincident with the axes of symmetric, bipolar jets. In all of the cases, the GRB isotropic equivalent energy (in photons) is $E = 10^{53}$ erg. For beamed emission, a trough appears in the light curve at $t \sim R(1 - \cos \theta_{\text{jet}})/c$. As θ_{jet} decreases, the width of the trough increases. The figures also show the afterglow light curves for comparison. For this particular configuration, dust echo bumps are visible with a brightness well above the afterglow, several weeks to months after the GRB.

For $\lambda_0 = 3.55$ μm and $\theta_{\text{jet}} = 22.5^\circ$, we compute light curves for different values of the viewing angle (Fig. 8). Even though this value of θ_{jet} is hardly typical of most GRBs, we adopt it as an illustration and as a matter of computational expediency. The main effect of an increasing ψ is to make the trough shallower, while lowering the light curve for $t \lesssim R/c$. Eventually, for $\psi = 90^\circ$, a bump emerges in place of the trough. These behaviors can be understood in the following manner: at $\psi = 0^\circ$, the echo surface at $\sim R/c$ samples the least *illuminated* dust; when this configuration is rotated by 90° , it now instead samples the most dust. Note that for Figs. 7 and 8, we apply a smoothing and interpolation procedure in places where numerical noise is clearly present, taking care not to alter the qualitative behavior of the light curves.

For a GRB observed from its onset until a time t_{obs} , one can measure the echo energy (per unit frequency),

$$E_\nu = \int_0^{t_{\text{obs}}} L_\nu dt. \quad (13)$$

We compute light curves for the range of rest frame wavelengths $1 \text{ nm} \leq \lambda_0 \leq 1 \text{ mm}$, for an isotropic fireball. Integrating these light curves till $t = t_{\text{obs}}$ yields the spectrum, which we obtain for two values of t_{obs} (Fig. 9). In the infrared, the echo is dominated

by thermal re-emission from graphite grains. Since re-emission is isotropic, the spectrum hardly changes with time. In the soft X-ray, dust grains preferentially scatter light forwards, causing the spectrum to be highly variable, being stronger at early and weaker at late times. By separating the dust echoes into thermal and scattered components (Fig. 9), we see that they peak at about $\lambda_{\text{peak}} = 3.55 \mu\text{m}$ (infrared) and 8.80 eV (extreme ultraviolet/soft X-ray), respectively. The former value justifies our earlier choice of $\lambda_0 = \lambda_{\text{peak}}$ in Figs. 7 and 8. Various studies have yielded different predictions for λ_{peak} : 2 μm (EB00), K band (R01) and 8 μm (Venemans & Blain 2001). The fact that these values differ is hardly surprising, as λ_{peak} depends sensitively on the adopted dust composition, the range of grain sizes and temperatures, as well as the cloud configuration. It is worthwhile to note that these calculations are for essentially static grain populations. By allowing the dust distribution to evolve, we include contributions from hotter grains which survive only for a very short time in the interstellar medium (Fig. 4). We also apply an extinction correction, $\exp(-\tau)$, due to the presence of a thin, post-burst dust layer, to our spectra; it is clear that this correction is negligible at $\lambda_0 = \lambda_{\text{peak}}$.

A striking observational feature of dust echoes from GRBs with symmetric, bipolar jets is the presence of two bumps, each corresponding to emission from the region illuminated by one of the two jets. This is an important difference from SN bumps that are expected to contribute only a single rebrightening. Furthermore, the temporal separation between the two peaks allows one to directly infer the opening half-angle, since the first bump appears at $t_1 \sim R(1 - \cos\theta_{\text{jet}})/c$ while the second emerges at $t_2 \sim 2R/c$. For a narrow jet, we have

$$\theta_{\text{jet}} \sim 2\sqrt{\frac{t_1}{t_2}}. \quad (14)$$

If the GRB does not sit in the center of the cloud, equation (14) becomes more complicated and we then need to use the relative brightnesses of the peaks to constrain the burst location.

3.2. OBSERVATIONAL PROSPECTS

For a region of size $\sim 3 \text{ pc}$ and density $n_{\text{H}} \sim 10^3 \text{ cm}^{-3}$, the luminosity of the dust echoes is $\sim 10^{27} \text{ erg s}^{-1} \text{ Hz}^{-1}$ at a wavelength of 3.55 μm , allowing them to sit above the afterglow light curve for time scales of about a month to over a year.

In Figs. 7 and 8, we display additional axes for the M magnitude of the echoes. At $\lambda_0 = 3.55 \mu\text{m}$, we need the source to be located at $z \approx 0.4$ in order to detect its light in the M band (5 μm). For on-axis GRB jets, the echo bumps have a magnitude of $M \sim 26 - 27$, straining the detection limits of ground-based telescopes, but well within the reach of IRAC

onboard the *Spitzer Space Telescope*. Specifically, for a cloud of $R = 3$ pc and $N_{\text{H}} = 10^{22}$ cm^{-2} , infrared echoes should be detectable with IRAC at 3.6 and 4.5 μm up to $z \sim 0.2$ (Fig. 10) and with NICMOS (in the J band) onboard the *Hubble Space Telescope* up to $z \sim 0.3$.

In the optical, the echoes are less bright, with expected magnitudes of $Rb \sim 30$ and $Vb \sim 30$. Figure 10 shows minimum flux thresholds for the *Very Large Telescope (VLT)* and demonstrates that optical echoes can be seen up to $z \sim 0.1$. Finally, in the X-ray, the echo flux is dominated by scattering — in the 0.1 to 1 keV band, we have $F_X \sim 10^{-16}$ $\text{erg cm}^{-2} \text{s}^{-1}$ at $z \sim 0.1$. Such a low flux is barely detectable with a long *Chandra* exposure, making the X-ray band an unattractive prospect in the search for dust echoes from the circumburst medium.

Extrapolating these results to different dust geometries is not straightforward. Naively, the dust luminosity scales as

$$L_{\text{echo}} \sim \zeta \frac{cE}{2R}, \quad (15)$$

where ζ hides the complexity of the time-dependent dust distribution. Equation (15) gives an optimistic scaling and should be used with caution. On one hand, ζ will be low for a very large cloud, since the grains will not reach very high temperatures. However, a very small region will also have a low ζ due to the fact that all of the dust is sublimated in the very first few fractions of a second by the burst radiation. Increasing the amount of dust increases ζ , but at the expense of causing residual absorption by dust in the cloud, delaying the echoes and thereby lowering their luminosity.

4. DISCUSSION

We have computed dust echoes due to scattering and thermal re-emission of dust by GRB sources. Our model allows for time-dependent dust destruction by both isotropic and beamed radiation from the GRB, as well as for any inclination of the jet axis with respect to the line of sight to the observer. Our source model assumes that the outer edges of the jets are sharp. Under these conditions and the assumption of symmetric, bipolar jets, a pair of bumps is expected in the light curve, an intrinsically different behavior from the possible presence of a single SN bump. This feature should qualitatively remain even if the jet is structured (Rossi, Lazzati & Rees 2002; Zhang & Mészáros 2002). The energy input in this case is a function of the angle from the jet axis — namely, $\epsilon \propto \Theta^{-k}$, where we typically have $1.5 < k \lesssim 2$. [However, we note that the numerical simulations of Morsony, Lazzati & Begelman (2006) allow for $k \gg 1$.] Due to the energy dependence with angle from the jet axis, dust is destroyed out to larger radii along the jet axis than in its wings. The range

of grain temperatures present is therefore expected to vary with azimuthal angle. The light travel paths of the photons differ, due to different geometries created by the destruction fronts. Thus, one expects varying observational features depending on the structure of the GRB jet.

Qualitatively, one can think of a structured jet as a superposition of a number of *non-structured* jets with different θ_{jet} . The component with the smallest opening half-angle, θ_{core} , forms the core of the structured jet, produces the brightest echo and displays a trough in its light curve at the earliest time. The net effect from summing all of the components is to form an echo light curve with a gentle decline at $t_{\text{core}} \sim R(1 - \cos \theta_{\text{core}})/c$, rather than a sharp transition to a trough. As a consequence, the first echo bump will likely be undetectable, since it lies at very early times and is outshone by the afterglow.

Observationally, we conclude that even echoes from moderate redshift events are hard to detect with present ground-based telescopes. Infrared observations with *Spitzer* and *Hubble* — and in the future with the *James Webb Space Telescope* — will detect echo components in GRBs out to $z \sim 0.3$. An intriguing prospect is the detection of orphan dust echoes, which are those from a misaligned jet. They are almost as bright as echoes from an on-axis GRB, but are not contaminated by the burst and afterglow radiation. Detecting such echoes in the optical light curves of supernovae may serve as the observational signature of off-axis, “phantom” GRBs (and their accompanying “orphan afterglows”), which are otherwise exceedingly difficult to detect.

We wish to thank: Peter Ruprecht and James McKown for steadfast and unwaivering technical support at JILA; Brian Morsony for illuminating discussions concerning structured jets; Enrico Ramirez-Ruiz for useful conversations regarding orphan afterglows; Richard McCray and Svetozar Zhekov for helpful comments and suggestions, following their careful reading of the manuscript. This work was partially supported by NASA Grants NAG5-12279 (K.H.) and NAS5-26555 (K.H.), and NSF Grant AST 0507571 (K.H., D.L. and R.P.).

REFERENCES

- Akerlof, C., et al. 1999, *Nature*, 398, 400
 Chevalier, R.A. 1986, *ApJ*, 308, 225
 Couderc, P. 1939, *Ann. d’Ap.*, 2, 271
 Dwek, E. 1983, *ApJ*, 274, 175
 Draine, B.T., & Lee, H.M. 1984, *ApJ*, 285, 89

- Draine, B.T., & Hao, L. 2002, *ApJ*, 569, 780
- Draine, B.T. 2004, *Astrophysics of Dust*, ASP Conference Series, 309, ed. A.N. Witt, G.C. Clayton, & B.T. Draine, 691
- Emmering, R.T., & Chevalier, R.A., 1989, *ApJ*, 338, 388
- Esin, A.A., & Blandford, R. 2000, *ApJ*, 534, L151
- Frail, D.A., et al. 2006, *ApJ*, 646, L99
- Frontera, F, et al. 2004, *ApJ*, 614, 301
- Fruchter, A., Krolik, J.H., & Rhoads, J.E. 2001, *ApJ*, 563, 597
- Henry, L.C., Greenstein, J.L. 1941, *AJ*, 93, 70
- Hjorth, J. et al. 2003, *Nature*, 423, 847
- Laor, A., & Draine, B.T. 1993, *ApJ*, 402, 441
- Lazzati, D., & Perna, R. 2002, *MNRAS*, 330, 583
- Lazzati, D., & Perna, R. 2003, *MNRAS*, 340, 694
- Mathis, J.S., Rumpl, W., & Nordsieck, K.H. 1977, *ApJ*, 217, 425
- Milgrom, M. 1987, *A&A*, 182, L21
- Moran, J.A., & Reichart, D.E. 2005, *ApJ*, 632, 438
- Morsony, B.J., Lazzati, D., & Begelman, M.C. 2006, *ApJ*, in press (astro-ph/0609254)
- Panaiteanu, A., & Kumar, P. 2000, *ApJ*, 543, 66
- Patat, F. 2005, *MNRAS*, 357, 1161
- Perna, R., & Lazzati, D. 2002, *ApJ*, 580, 261
- Perna, R., Lazzati, D., & Fiore, F. 2003, *ApJ*, 585, 775
- Reichart, D.E. 2001, *ApJ*, 554, 643
- Rossi, E., Lazzati, D., & Rees, M.J. 2002, *MNRAS*, 332, 945
- Schaefer, B. 1987, *ApJ*, 323, L47
- Schaefer, B. 1987, *ApJ*, 323, L51
- Sparks, W.B. 1994, *ApJ*, 433, 29
- Stanek, K. et al. 2003, *ApJ*, 591, L17
- Sugerman, B.E.K. 2003, *AJ*, 123, 1939
- Waxman, E., & Draine, B.T. 2000, *ApJ*, 537, 796

- Williams, P. M., van der Hucht, K. A. & The, P. S. 1987, *A&A*, 182, 91
- Venemans, B.P., & Blain, A.W. 2001, *MNRAS*, 325, 1477
- Xu, J., Crofts, A.P.S., & Kunkel, W.E. 1994, *ApJ*, 435, 274
- Xu, J., Crofts, A.P.S., & Kunkel, W.E. 1995, *ApJ*, 451, 806
- Zhang, B., & Mészáros, P. 2002, *ApJ*, 571, 876

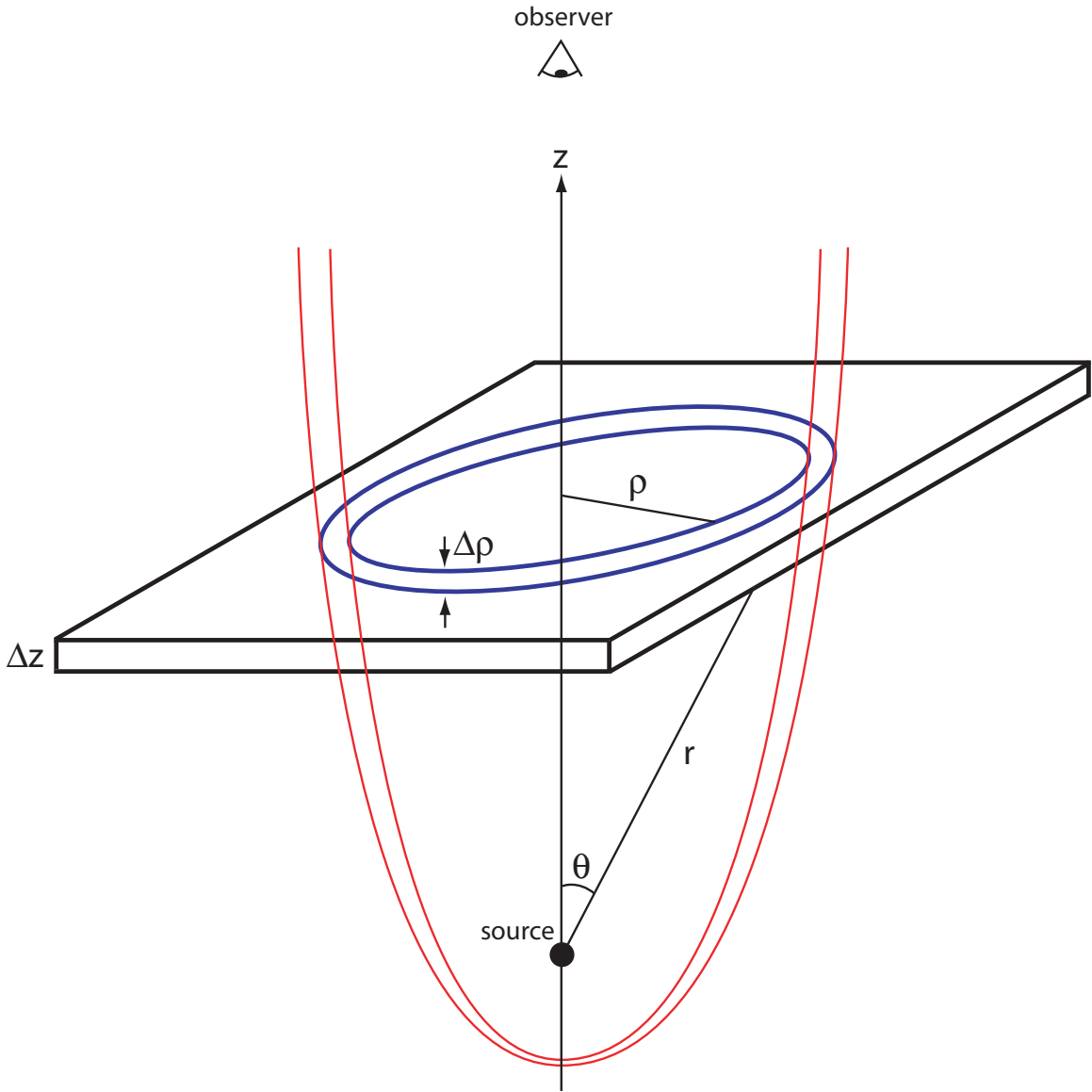


Fig. 1.— Dust echo geometry, adopted from Sugerman (2003).

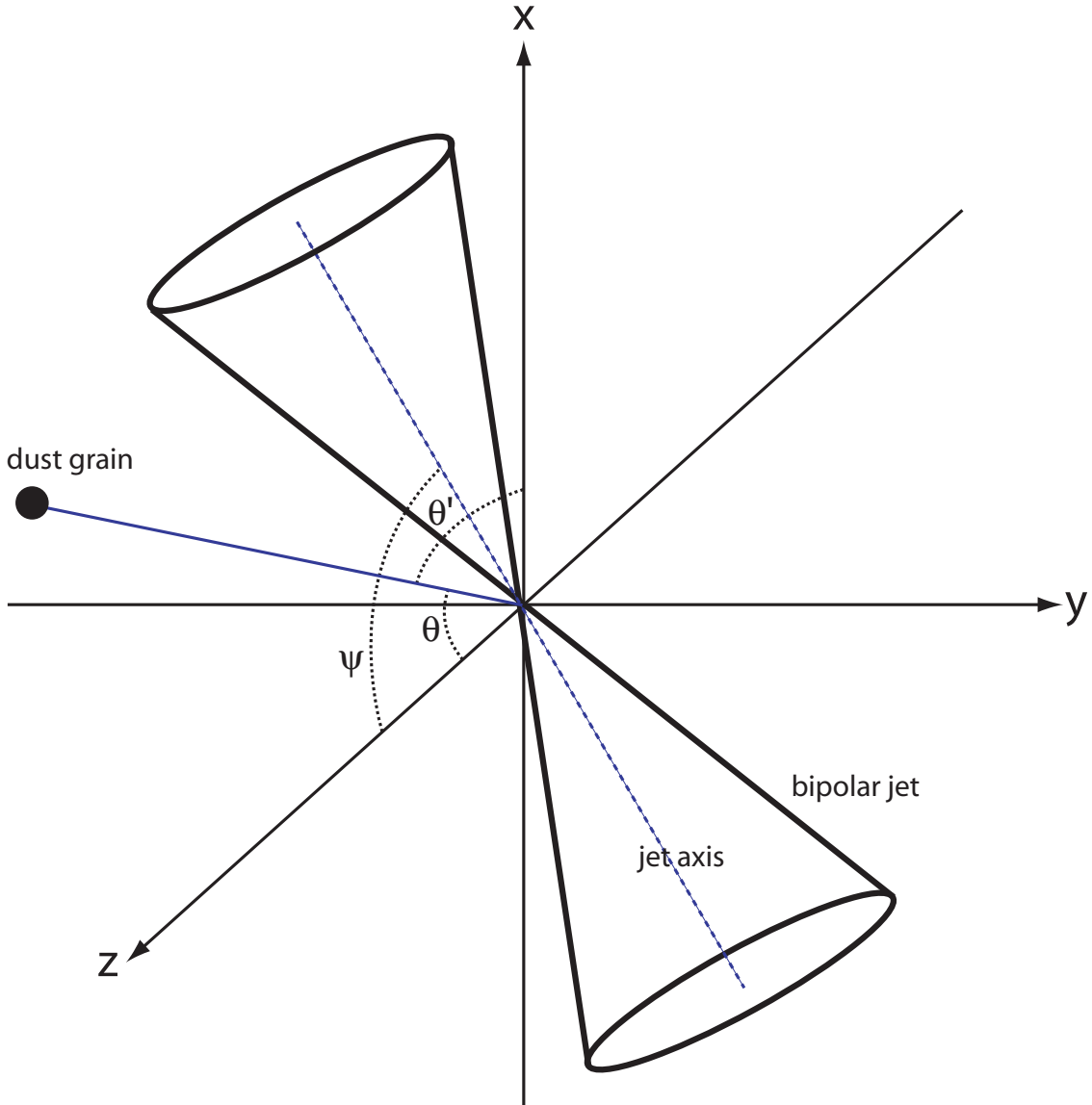


Fig. 2.— Geometry for GRB beaming. A bipolar jet of opening half-angle θ_{jet} (not displayed in the diagram) is positioned at a viewing angle of ψ between the jet axis and the light of sight (z -axis). While the jet axis is located in the x - z plane, the dust grain shown is generally not found in the same plane; θ is the scattering angle. Knowledge of the occurrence angle, θ' , allows one to determine if the light curve contribution from a given dust grain should be included (see text). Also not shown is the angle ϕ , which is the azimuthal angle about the line of sight.

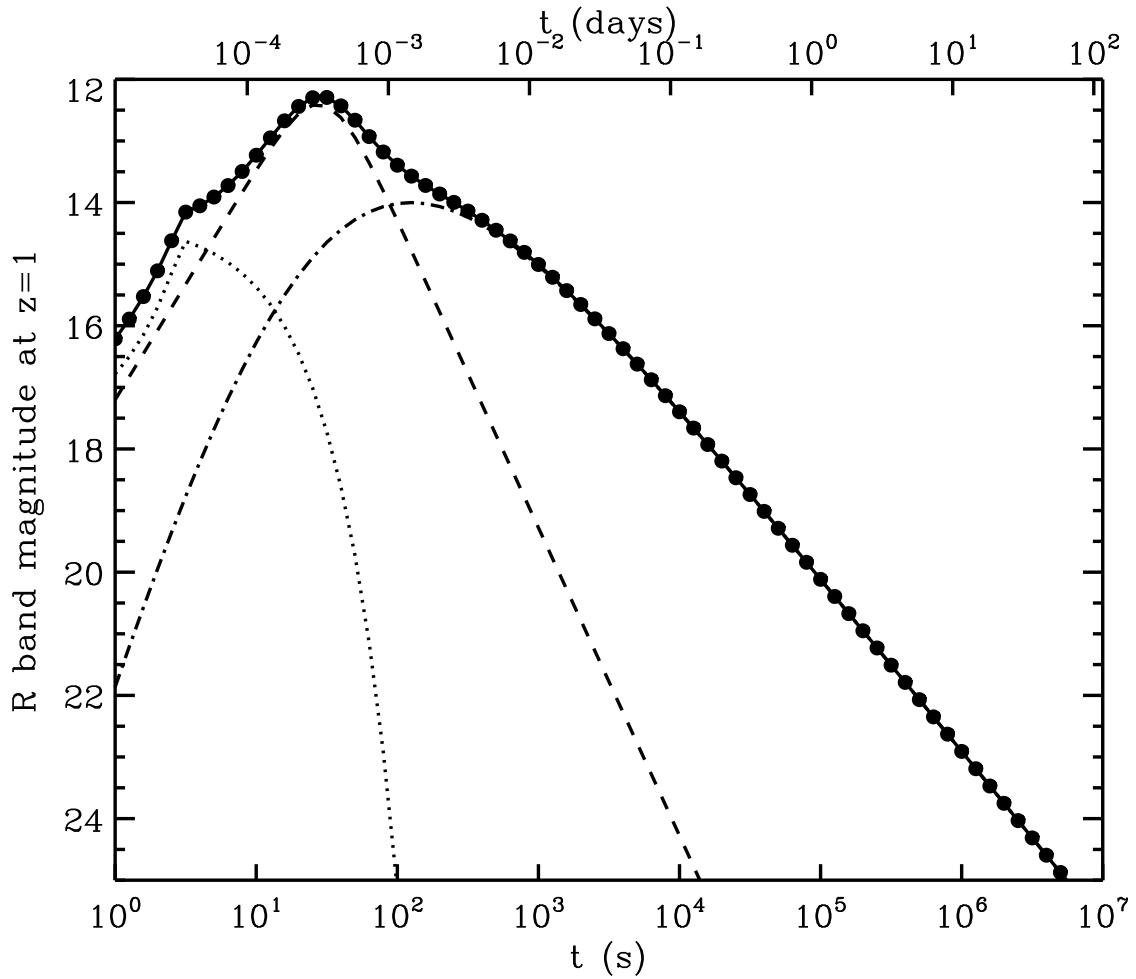


Fig. 3.— R band light curve according to our GRB model for an event at $z = 1$. The solid line with dots shows the total light curve, while dotted, dashed and dot-dashed lines represent the prompt, optical flash, and afterglow emission, respectively.

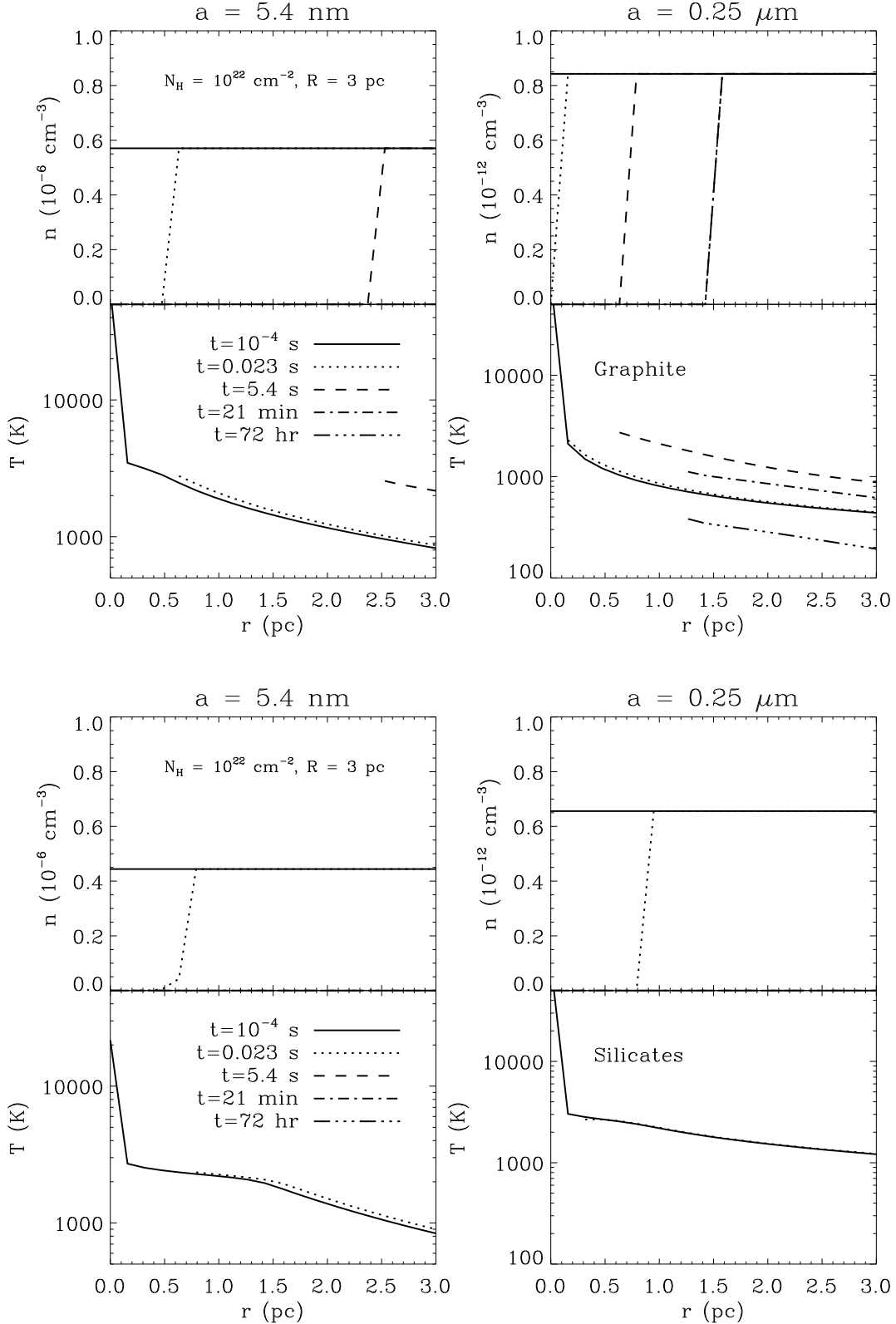


Fig. 4.— Input number densities, n , and temperatures, T , for two representative grain sizes and at different times since the GRB, generated using the dust code of Perna and Lazzati (2009). Shown are graphite (top) and silicate (bottom) grains.

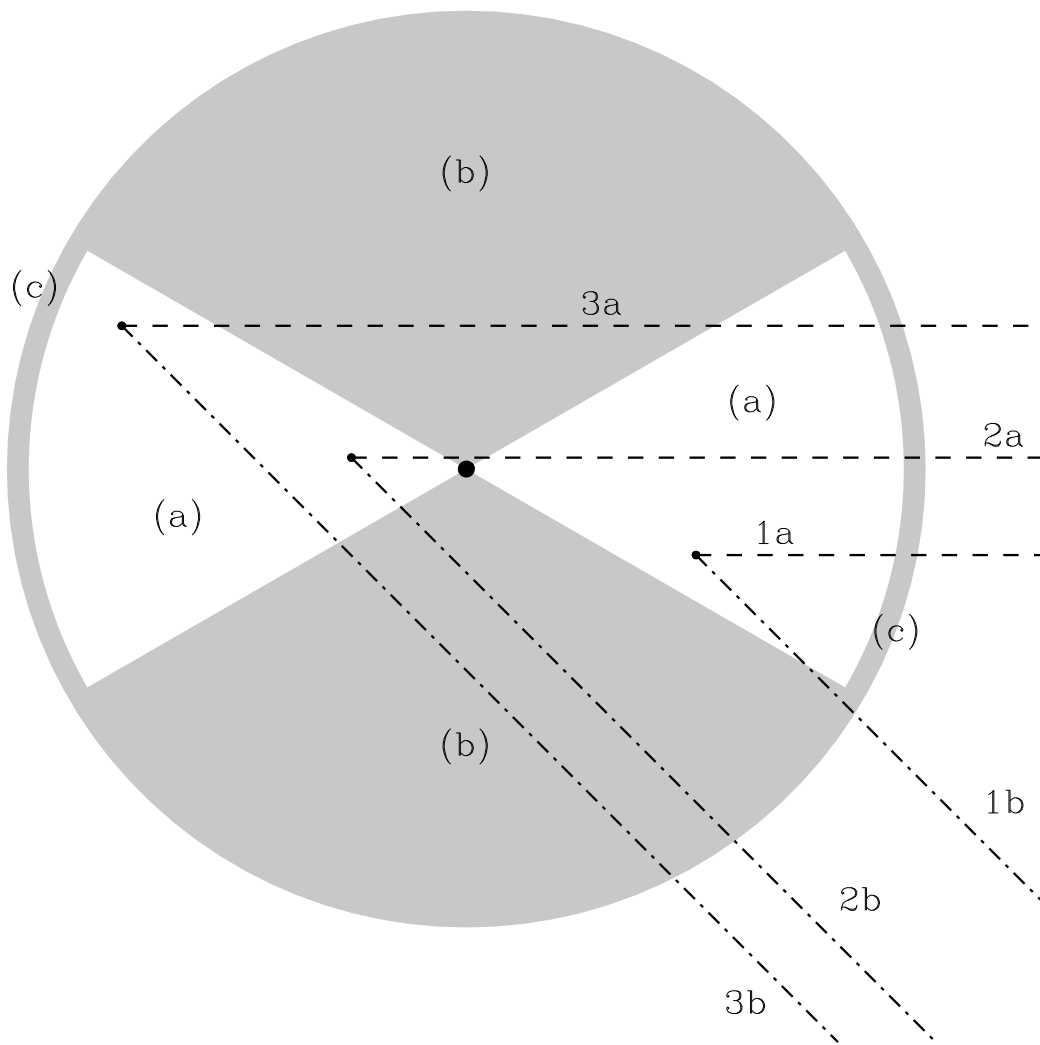


Fig. 5.— Cartoon showing the final configuration of a cloud illuminated by a beamed GRB — three regions can be identified in the cloud. Region (a) has all of the dust completely destroyed by the burst, yielding no residual opacity. Region (b) is outside the beaming cone and holds the unmodified dust populations. Region (c) is a layer of dust left on the outskirts of the cloud; it is not a general outcome of the simulations as region (a) extends all the way to the edge for more compact clouds. Dashed lines show several paths of re-directed photons from the illuminated dust towards an on-axis observer. The various paths range from almost clear (1a) to largely obscured ones (3a). Dot-dashed lines show the paths to an observer located outside the cone — for such paths, relatively more extinction is generally experienced (cfr. 123a with 123b).

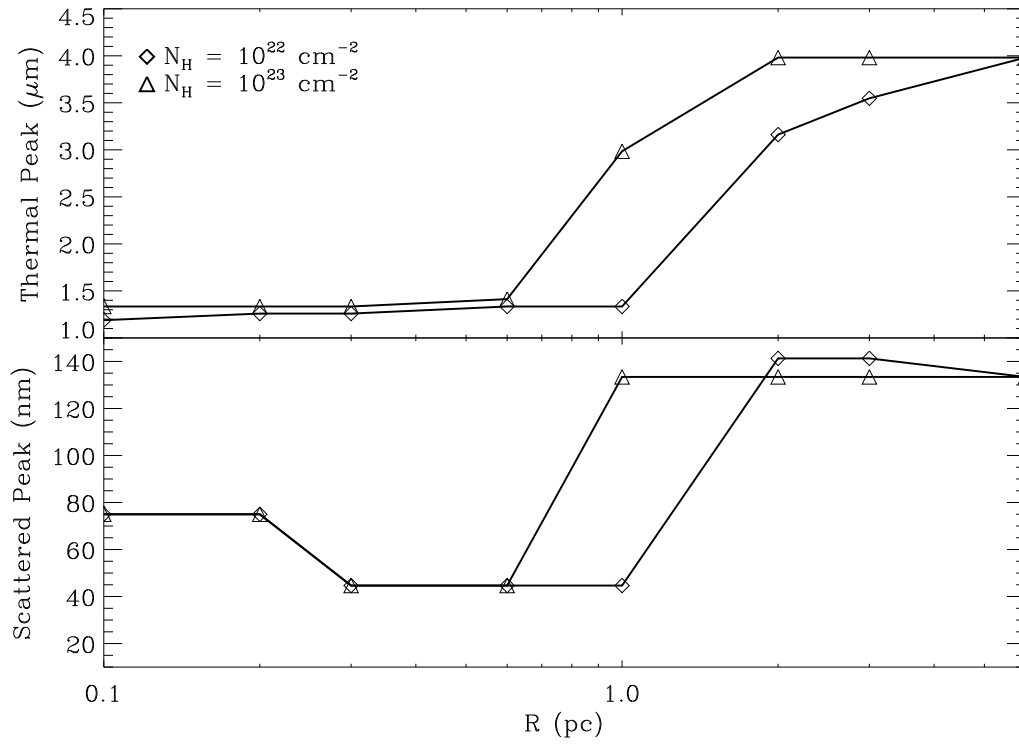


Fig. 6.— Thermal (top) and scattered (bottom) peak wavelengths as a function of the cloud radius R for hydrogen column densities $N_{\text{H}} = 10^{22}$ and 10^{23} cm^{-2} . Note that these are *intrinsic* wavelengths for which no extinction correction has been applied to the spectra.

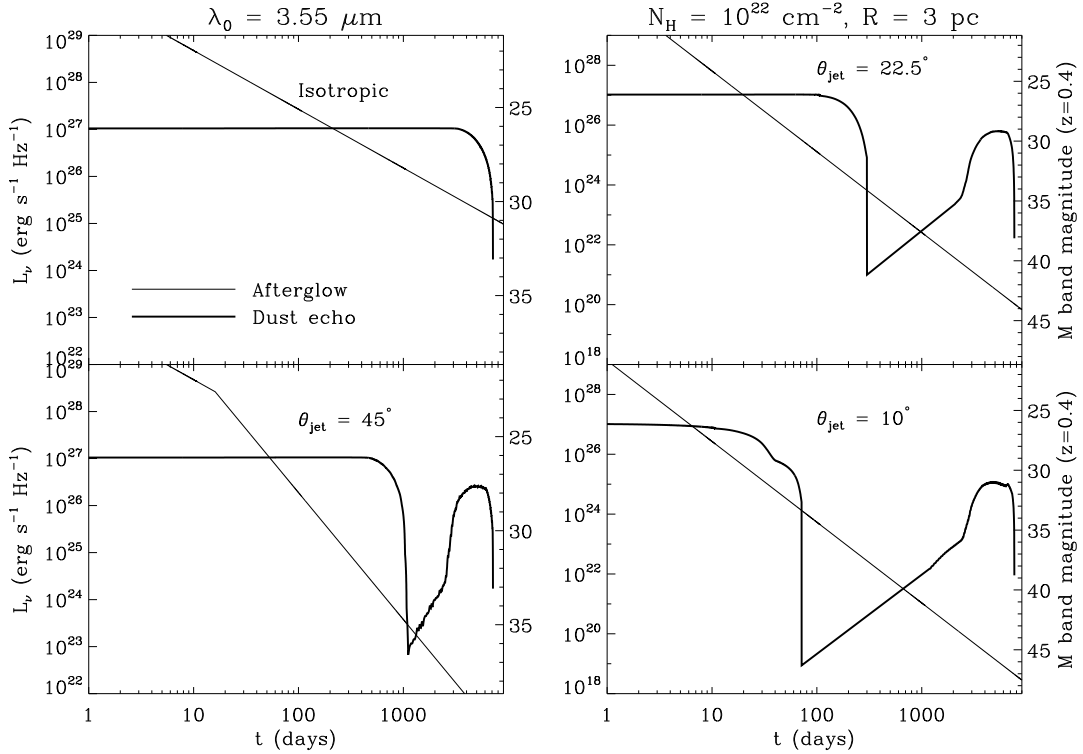


Fig. 7.— Dust echo light curves for on-axis GRBs. Isotropic and beamed ($\theta_{\text{jet}} = 10^\circ, 22.5^\circ$ and 45°) emission are both considered. The corresponding afterglows are plotted for comparison and $2R/c \sim 2400$ days.

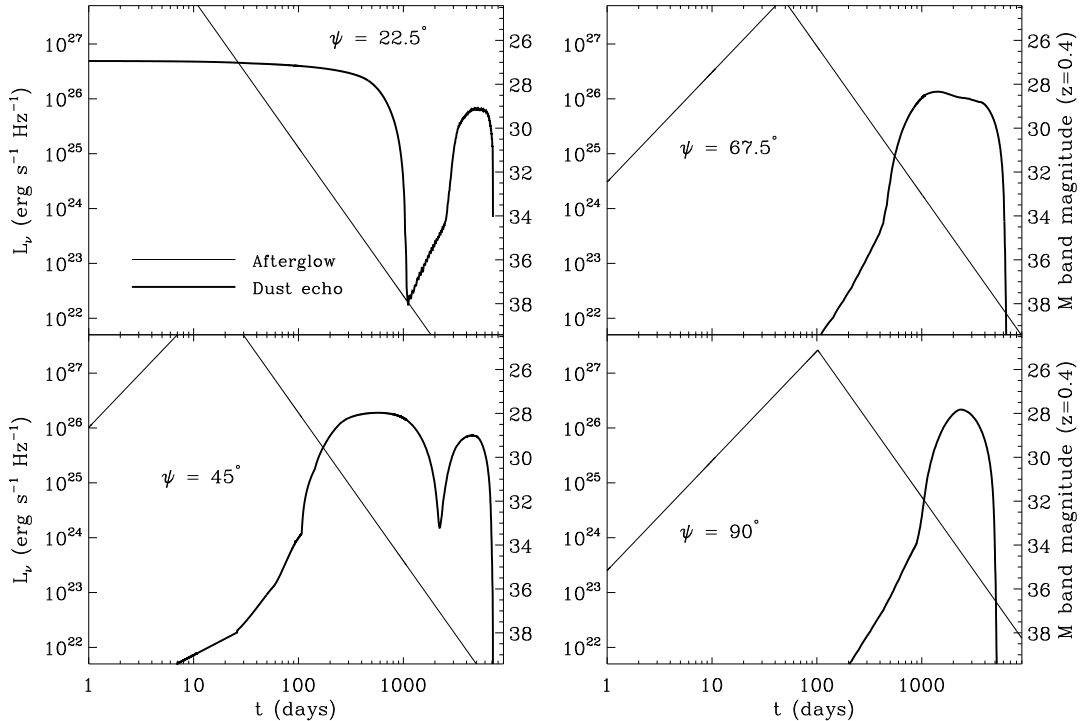
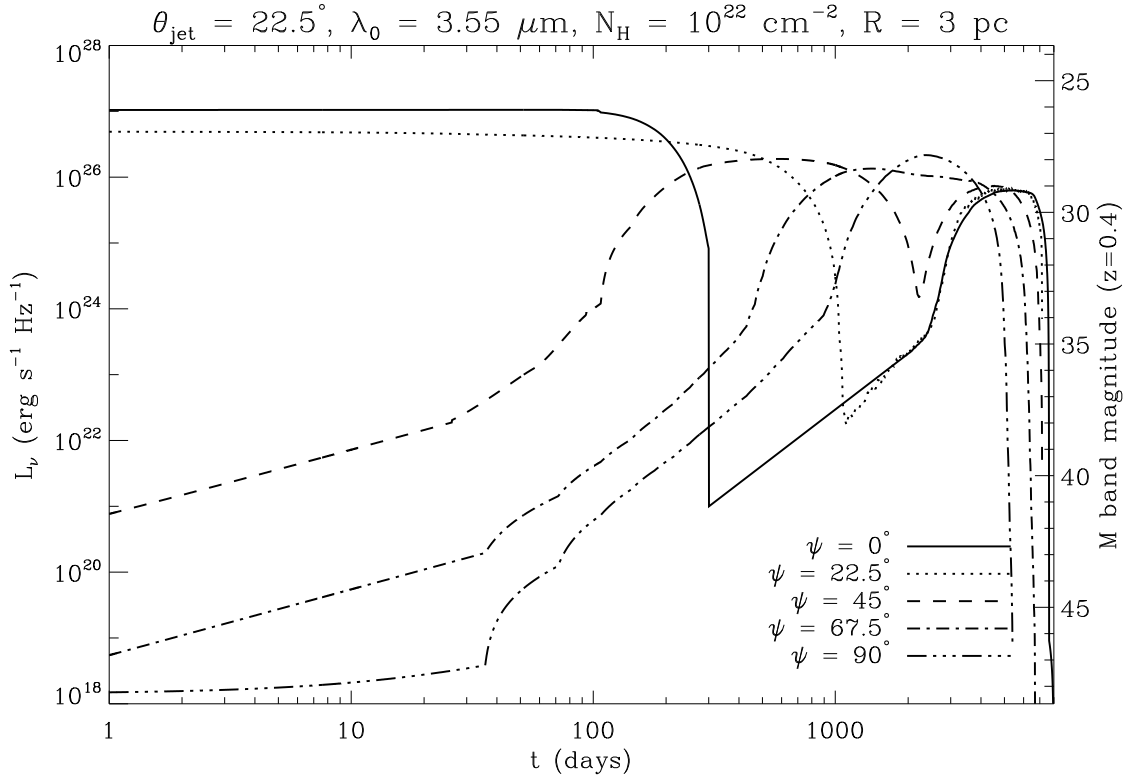


Fig. 8.— Top: Dust echo light curves for jet opening half-angle $\theta_{\text{jet}} = 22.5^\circ$ and various values of the viewing angle, ψ . Bottom: Light curves with different ψ plotted against the corresponding dip in afterglow.

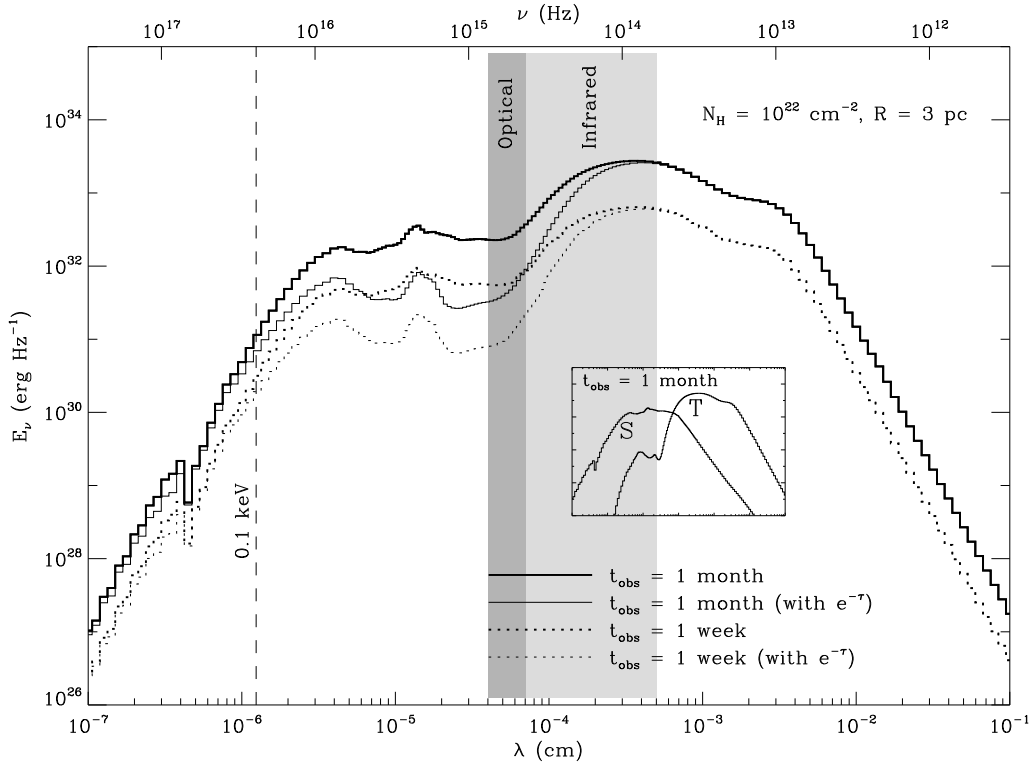


Fig. 9.— Dust echo spectrum integrated from $t = 0$ to t_{obs} . As an illustration, the insert shows the separated scattered (denoted by “S”) and thermal (denoted by “T”) components for $t_{\text{obs}} = 1 \text{ month}$. Also shown are the spectra with the $\exp(-\tau)$ extinction correction applied.

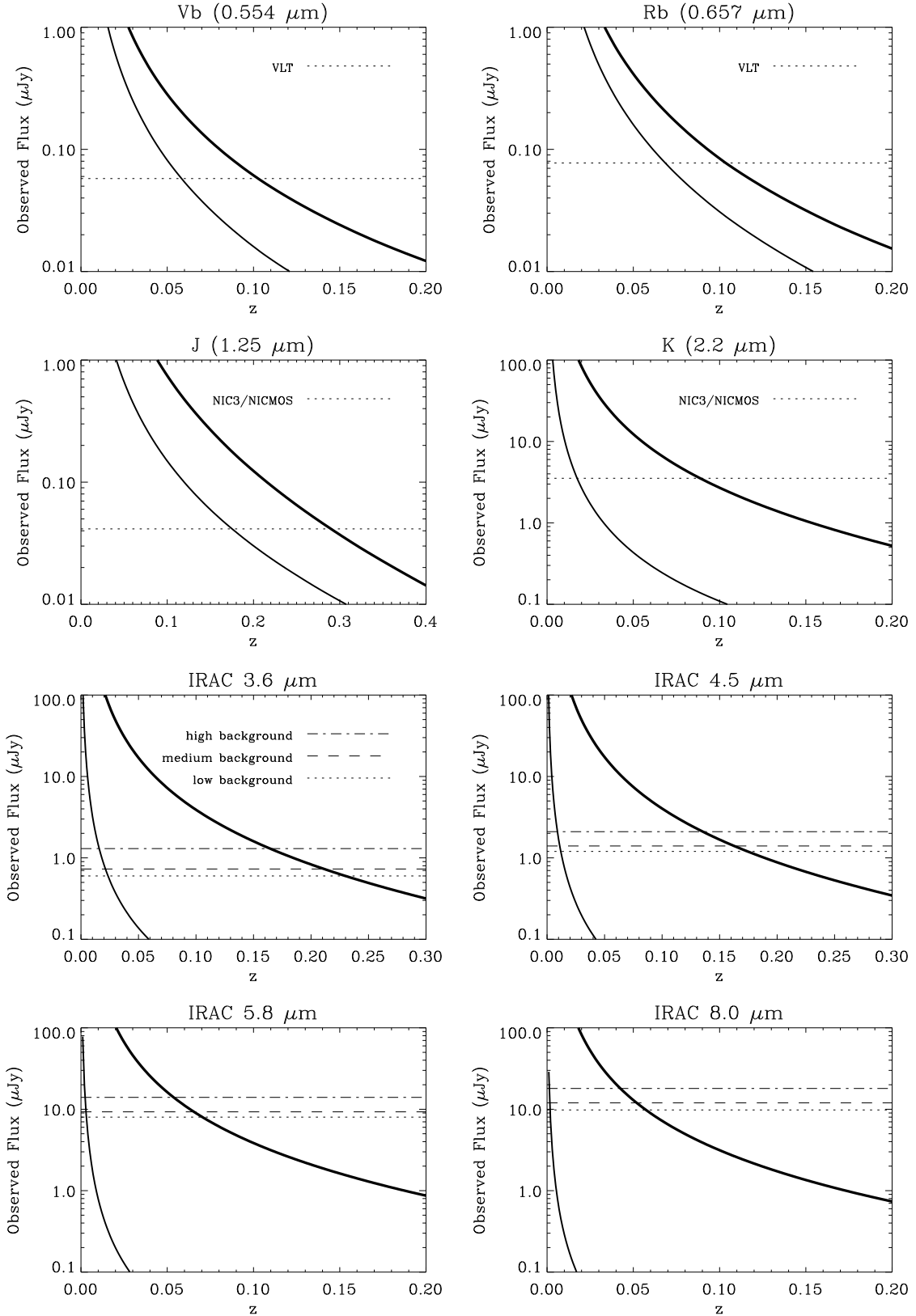


Fig. 10.— Time-averaged, observed echo flux, from isotropic fireballs, as a function of redshift, z , with the extinction correction applied. Shown are two $N_{\text{H}} = 10^{22} \text{ cm}^{-2}$ cloud models for comparison — with the thin and thick lines representing $B_{\text{c}} = 1$ and 3, respectively. We